Cellulose (2020) 27:3181–3195
https://doi.org/10.1007/s10570-020-03015-x

ORIGINAL RESEARCH

Superior crack initiation and growth characteristics of cellulose nanopapers

Chengyun Miao · Haishun Du · Mahesh Parit · Zhihua Jiang · Hareesh V. Tippur · Xinyu Zhang · Zhongqi Liu · Junhao Li · Ruigang Wang

Received: 19 December 2019 / Accepted: 20 January 2020 / Published online: 31 January 2020
© Springer Nature B.V. 2020

Abstract In this work, tension and fracture behaviors of cellulose nanopaper (CNP) made from two different preparation approaches are comparatively studied. The CNP are prepared by casting (or C-CNP) and filtration (or F-CNP) of CNF suspension. The resulting CNP are mechanically characterized using the vision-based full-field optical method of Digital Image Correlation. Tension tests show that F-CNP has a higher strength and greater nonlinearity than the C-CNP. The crack initiation and growth characteristics of the two types of CNP are investigated using optical measurements. The data are analyzed under small-scale-yielding conditions to quantify the fracture parameters such as stress intensity factors and energy release rates at crack initiation as well as during crack growth. The results indicate that both C-CNP and F-CNP show significant crack growth resistance in the post-crack initiation regime. The F-CNP particularly offers substantial resistance to crack growth relative to the C-CNP demonstrating that filtration is the preferred method to make CNP with higher tensile strength and better fracture properties.

Chengyun Miao and Haishun Du contributed equally to this work.

Electronic supplementary material The online version of this article (https://doi.org/10.1007/s10570-020-03015-x) contains supplementary material, which is available to authorized users.

C. Miao · H. V. Tippur (✉)
Department of Mechanical Engineering, Auburn University, Auburn, AL 36849, USA
e-mail: tippuhv@auburn.edu

H. Du · M. Parit · Z. Jiang · X. Zhang (✉)
Department of Chemical Engineering, Auburn University, Auburn, AL 36849, USA
e-mail: xzz0004@auburn.edu

Z. Liu · J. Li · R. Wang
Department of Metallurgical and Materials Engineering, The University of Alabama, Tuscaloosa, AL 35487, USA

Graphic abstract

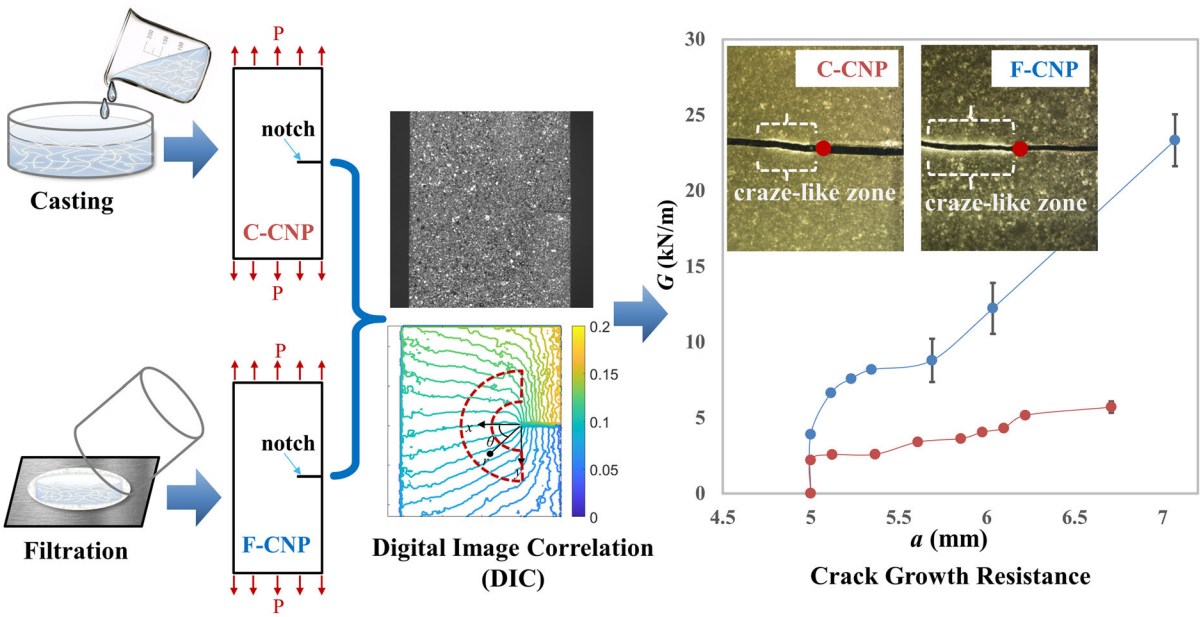

Keywords Cellulose nanopaper · Cellulose nanofibrils · Filtration and casting · Fracture properties · Crack initiation and growth · Digital Image Correlation

Introduction

Cellulose nanofibrils (CNFs), an advanced bionanomaterials produced mainly from lignocellulosic biomass, have attracted a great deal of attention of both academics and industries in recent years (Du et al. 2016; Rol et al. 2019; Bian et al. 2019). CNFs possess unique nanostructure and outstanding mechanical properties such as high elastic modulus, high specific surface area, high thermal stability, excellent chemical resistance, tunable surface chemistry, as well as biocompatibility and biodegradability (Du et al. 2018; Xie et al. 2018). Therefore, CNFs have great application potential in the fields of paper and packaging coatings (Abdul Khalil et al. 2016; Liu et al. 2017), wastewater treatment (Abouzeid et al. 2018; Mohammed et al. 2018), biomedical implants (Du et al. 2019; Luo et al. 2019), reinforcing nanofillers for various polymers (Kargarzadeh et al. 2018; Zheng et al. 2019; Bian et al. 2018a), and many others (Jiang et al. 2018; Thomas et al. 2018; Zhu et al. 2016).

Due to the large specific surface area, high aspect ratio and semi-crystalline structure, CNFs exhibit remarkable tendency to easily entangle with each other and thus form flexible and mechanically stable thin film, which is usually named cellulose nanopaper (CNP) (Benítez and Walther 2017; Hu et al. 2018). It is noteworthy that CNP has excellent mechanical properties, high dielectric constant, high thermal durability, as well as tunable optical properties (Brhoum et al. 2017; Operamolla et al. 2018; Wang et al. 2018). Moreover, CNP possesses extremely small thermal expansion coefficient (< 10 ppm/K), which is smaller than that of glass (50 ppm/K) and much smaller than that of most moldable plastics (approximately 200 ppm/K) (Sun et al. 2015). These unique properties make CNP a promising material for various multifunctional and high-end applications such as organic solar cell (Cheng et al. 2018; Nogi et al. 2015), visual display substrates (Jung et al. 2015; Zhu et al. 2013), energy storage electrode (Chen et al. 2018; Xing et al. 2019), etc.

CNP is usually prepared from CNF suspension by a self-assembly process in which the solvent is removed and the CNF finally form the CNP (Benítez and

Walther 2017; Bian et al. 2018b). Casting and filtration are two popular approaches for CNP production (Qing et al. 2015). Among them, casting is a simple but time-consuming process, by which CNF suspension is usually kept in an open Petri dish, and the solvent is allowed to evaporate, finally leaving the self-assembled CNP (Aulin et al. 2010). Normally, a slow drying rate is necessary to reduce wrinkling problem and make flat, and uniform CNP (Parit et al. 2018). This process usually takes several days to obtain final CNP. Filtration, which is similar to a papermaking process, is a relatively fast method to prepare CNP. Typically, filtration process involves two separate operations: (a) filtration of CNF suspension under vacuum or pressure and (b) drying (e.g. air-drying, oven-drying, hot-pressing) of thus obtained CNF gels (Mautner et al. 2015; Sehaqui et al. 2010). The total time of filtration process is reported to be a few hours instead of days, which is much faster than the casting method. It is noteworthy that the CNP preparation procedures affect the properties (e.g., mechanical, optical) of the resulting CNP. For example, Qing et al. (2015) investigated the effect of processing conditions on the mechanical and physical properties of CNP. It was found that the CNP prepared by casting showed lower tensile strength than the one produced by filtration. The authors recommended filtration approach, which was able to produce CNP of high mechanical strength, good light transmittance, minimal defects, as well as relatively smaller effort. In another study, Yang et al. (2017) compared the effects of preparation approaches on optical properties of the self-assembled CNP. Interestingly, they found the CNP produced by casting exhibited much smoother surface and higher light transmittance than that of the CNP prepared by filtration. However, up to now, there is no report on the comparison of mechanical properties, particularly the fracture characteristics of crack growth in CNP, by different preparation approaches.

Recently, some research has been reported on the fracture behavior of CNP. Zhu et al. (2015) found that the fracture toughness (also called the crack initiation toughness) of CNP increased with the ultimate tensile strength. This was attributed to the breaking of hydrogen bonds among cellulose nanofibers at crack initiation, but they re-form or tends to heal when the crack extends. A companion atomistic simulation was used by the authors to support their reasoning. Mao et al. (2017) comparatively investigated the fracture characteristics of CNP, conventional printing paper, and buckypaper. They showed that both fiber pull-out and inter-fiber interactions play important role in the fracture property of CNP. Meng et al. (2017, 2018) developed crack-bridging models for CNP to study the effects of bridging toughening of nanofibrils, and nanofiber orientations on the macroscale fracture toughness. However, all the reported works on fracture of CNP to date have primarily focused on the so-called fracture toughness, which generally corresponds to the property at the crack initiation. Fracture performance during crack growth, on the other hand, is equally if not more important in CNP in light of potential micro/nanoscale toughening mechanisms related to abrupt versus graceful failure events. Thus, there is a need to investigate the entire fracture process in CNPs as fracture of fibrous structures may behave quite differently in the pre- and post-crack initiation regimes. In fact, it is well-known in conventional fiber reinforced polymer composites that the bridged fibers across the crack faces produce higher crack growth resistance in the post-crack initiation regime during the fracture process (Miao and Tippur 2019). Hence, it is critical to study the entire fracture process in CNP made from different processing methods.

Digital Image Correlation (DIC) technique is quite popular due to the advantages such as its ability to quantify deformations in the entire region-of-interest (ROI), which can be subsequently used to quantify mechanical properties (Chu et al. 1985). Diaz et al. (2013) utilized DIC to measure thermal expansion of cellulose nanocrystal (CNC) films to characterize the coefficient of thermal expansion. Shrestha et al. (2017) determined coefficient of hygroscopic swelling of CNC films based on the strain changes measured by DIC. Zhao et al. (2017) investigated in-plane strain fields on the tensile CNP using DIC. However, to the best of our knowledge, research on crack growth studies in CNP using DIC is currently lacking.

Motivated by the above factors, the present study is aimed at investigating the entire fracture behaviors of CNP produced by two different processes namely casting and filtration. The experimental details of the two types of CNP made by these two methods are introduced first. Next, the as-prepared CNPs are characterized using tension and quasi-static fracture tests. It includes a first-time study of the entire fracture process, crack initiation as well as growth behaviors. Experimental results including tensile properties and

fracture parameters along with fractography are further discussed. Finally, the major results of this research are summarized. This study will be beneficial to the future design of functional CNP with desirable fracture properties.

Experimental

Materials

Cellulose nanofibers (CNF) were obtained in an aqueous gel form with a concentration of approximately 3 wt% from University of Maine, USA. (Lot Number U31). The CNF were produced from bleached softwood kraft pulp (with the composition of around 85% cellulose, 15% hemicellulose and less than 0.1% lignin) by a mechanical grinding process without any chemical modification (Wang et al. 2019). Specifically, bleached softwood kraft pulp aqueous suspensions were circulated through a refiner until the fines content was over 90% as determined by laser diffraction as fibers smaller than 200 microns (Sun et al. 2019). Fig. S1 shows the morphology and diameter distribution of the CNF used in this study, we can see that the CNF display a wide diameter distribution from 18 nm to more than 200 nm and the length of up to several hundred microns. XRD pattern (Fig. S2) of the CNF displays diffraction peaks at 2θ = 15.1°, 16.5°, 22.6° and 34.6°, which are corresponding to the (1–10), (110), (200) and (004) crystallographic planes of characteristic diffraction peaks of cellulose Iβ.

CNP preparation by casting

The CNP produced by casting was named as C-CNP, and the C-CNP was prepared by using a standard casting method (Yang et al. 2017). The schematic of casting method is shown in Fig. 1a. Briefly, the CNF gel was diluted to a concentration of 0.5 wt% by DI water. The diluted CNF suspension was well mixed by stirring for 1 h. Then, 200 mL diluted CNF suspension was poured into a polypropylene Petri dish (diameter = 150 mm) with a smooth bottom and dried at room temperature for a few days. Finally, the dried CNP was kept in a vacuum oven at 80 °C for 24 h to eliminate residual moisture.

CNP preparation by filtration

The CNP produced by filtration was named as F-CNP. The preparation of F-CNP was carried out using the standard method developed by Parit et al. (2018). The schematic of filtration method is shown in Fig. 1b. Briefly, the CNF gel was diluted to aqueous suspensions of 1 L based on total weight of 1 g of CNF per F-CNP. The mixture was magnetically stirred for 2 h before introducing it to the British handsheet maker for preparing the F-CNP through filtration under suction. After filtration, the CNF gel was pressed using the couch roll five times by placing a layer of Nylon-polyester filter bag fabric, two pieces of blotting papers and a couch plate on top. This initial pressing removed the significant amount of residual water and enabled the CNP formation. The resultant CNP was removed from the handsheet maker metal screen by removing the couch plate, wet blotting papers from top but keeping the fabric cloth intact. It was then kept on a couch plate with a couple of blotting papers on the top and pressed in a cold press at a pressure of 345 kPa (50 psig) for 2 min. Same procedure was performed by flipping over CNP and replacing the blotting papers. After this step most of the water was removed from the CNP. The pressing in contact with the metal plate increased the smoothness of the resulting CNP. The CNP along with both fabric cloths was placed on a couch plate and inserted between two drying rings to carry out the restricted drying at room temperature for 24 h. The restricted drying carried out in this manner reduces the fiber shrinkage upon drying. The dried CNP was then kept in a vacuum oven at 80 °C for 24 h to eliminate residual moisture.

Tension tests

The elastic and tensile failure characteristics of both C-CNP and F-CNP were first investigated by performing uniaxial tension tests. The specimens were cut into dumbbell or dog-bone shaped geometry from CNP, as shown schematically in Fig. S3a. A strategy to grip thin specimens, 60 ± 3 μm for C-CNP and 40 ± 3 μm for F-CNP, had to be developed as direct gripping using standard steel grips of the testing machine would not only damage the CNP but potentially cause slippage during tests. Therefore, each specimen was end-tabbed by gluing it to two 25 mm × 25 mm × 3 mm polycarbonate plates, as

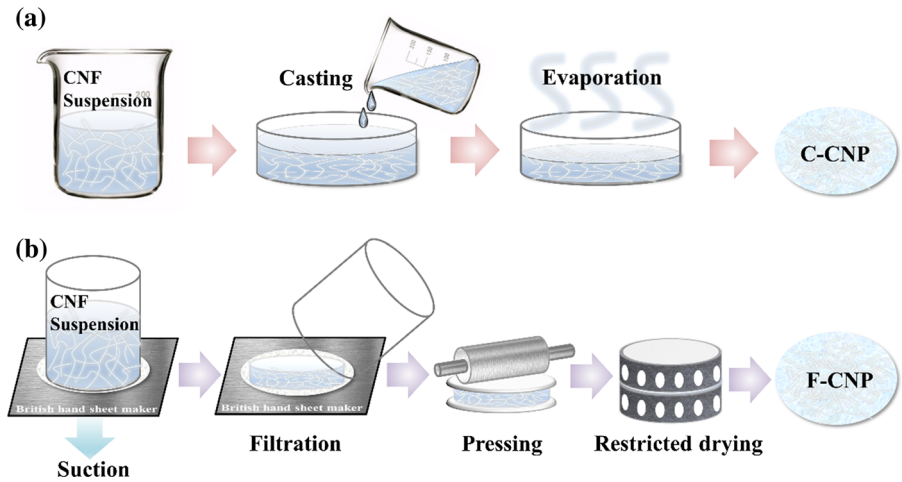

Fig. 1 Schematic of casting (**a**) and filtration (**b**) methods

shown in Fig. S3b. The specimens were also sprayed with alternating mists of black and white speckles to measure biaxial strains in order to evaluate the Poisson's ratio of CNP using 2D Digital Image Correlation (DIC) approach by measuring the longitudinal and transverse normal strains in the specimen gage section during tension tests. Sufficient precaution was exercised to prevent speckle coating from reinforcing the CNP. A photograph of the experimental setup used for performing DIC (Chu et al. 1985) is shown in Fig. S4. An Instron 4465 universal testing machine operating in displacement-control mode (crosshead speed = 3 mm/min) was used to conduct the tests. The load–deflection data were recorded up to complete specimen failure. Simultaneously, a Point Grey digital camera fitted with a Nikon 70–300 mm lens and adjustable bellows was used to photograph speckles on the specimen surface during deformation. Three specimens of each type of CNP were tested.

Fracture tests

The fracture mechanics of both C-CNP and F-CNP were studied next. Again, the DIC method was utilized for mapping the surface deformations. The single edge notched (SEN) specimens, schematically shown in Fig. S5 and prepared in the same way outlined in the tension tests, were loaded using Instron 4465 testing machine in displacement control mode (crosshead speed = 2 mm/min). The edge notches of 5 mm length were cut into these samples prior to the tests using a sharp razor blade. The experimental setup used was the same as the one shown in Fig. S4. The load–deflection data were recorded both up to crack initiation and during crack growth phases. Simultaneously a Point Grey digital camera fitted with a Nikon 70–300 mm lens and adjustable bellows was used to record speckles on the specimen surface around the crack-tip. These images (2048×2048 pixel^2) were recorded at 10 frames per second during tests. The load level for each image was corroborated subsequently from the load–deflection data including the ones at crack initiation, during stable crack growth, and unstable failure.

Optical microscopy

The fractured specimen edges of C-CNP and F-CNP were observed by using a KEYENCE VHX-6000 series microscope.

Scanning electron microscopy (SEM)

The morphology of freeze-dried CNF and fractured surfaces of C-CNP and F-CNP were observed by using a scanning electron microscope (SEM, JEOL7000) at 15.0 or 20.0 kV.

Results and discussion

Tension tests

The stress–strain responses of C-CNP and F-CNP are shown in Figs. S6a and b, respectively. It can be observed from the figures that the curves show an initial linear elastic region followed by a substantial nonlinear region prior to an abrupt specimen failure. The C-CNP specimens failed at lower strains and stress values when compared to their F-CNP counterparts. The C-CNPs failed at strains in the range of 2.2–3.9% with a relatively large variance between specimens. The F-CNP specimens, on the other hand, failed at strains in the range 3.7–4.4% with a smaller variance between specimens. In the former cases, the samples close to the edge of the Petri dish failed at a lower strain when compared to the one towards the center with the intermediate value corresponding to the sample in between the other two. The nonuniform solvent evaporation process over the entire film during material preparation close to the edges versus the center in C-CNP is a likely contributor to this variance. In F-CNP cases, however, the lack of solvent evaporation during material preparation could be an advantage in this regard. From the stress–strain plots, the elastic modulus for each specimen was determined as the slope of the stress–strain curves in the 0–0.1% strain range. The average values calculated for C-CNP and F-CNP are summarized in Table 1. The primary (longitudinal) and secondary (lateral) normal strain fields measured from DIC for C-CNP specimen S2 at two select stress levels, one in the linear and another in the nonlinear portion, are shown in Fig. S7. It can be observed that the strains are distributed rather uniformly over the entire specimen in both the linear and nonlinear regimes of the test. Plots of transverse strains versus longitudinal strains of C-CNP and F-CNP were also obtained from DIC and are plotted in Figs. S8a and b, respectively. The Poisson's ratio was then estimated using a linear regression of the data. The average Poisson's ratios of approx. 0.28 for C-CNP and 0.23 for F-CNP, thus obtained are also included in Table 1. Additionally, the average strength and strain-at-failure are included in the table. It can be observed that the elastic moduli of C-CNP and F-CNP ($\sim$ 10.8 GPa) are rather close to each other. Interestingly, these values are much higher than those for engineering polymers which typically are in the 2–4 GPa range. Regarding the failure characteristics, on the contrary, C-CNP has a lower average strength (79 $\pm$ 8 MPa) when compared to the F-CNP counterpart (90 $\pm$ 8 MPa), suggesting that the filtration method leads to mechanically stronger CNP relative to the casting method. Such improvement in tensile strength of F-CNP is probably attributed to the increased in-plane orientation of nanofibers and density of the nanopaper (Sehaqui et al. 2010), which is due to the cold pressing and restricted drying employed during its preparation. The higher density of F-CNP compared to the C-CNP counterpart could be used as evidences for this speculation (see Table S1).

Fracture tests

The load versus crosshead displacement curves of C-CNP and F-CNP samples from fracture tests are shown Fig. 2a and b, respectively. It can be observed from the plots that C-CNP specimens (60 $\pm$ 3 μm thick) failed at significantly lower crosshead displacements when compared to F-CNP specimens (40 $\pm$ 3 μm thick). Furthermore, these responses do not show a sudden drop in load typical of brittle fracture. Instead, a modest plateau region of stable crack growth, highlighted by a solid (blue) circle for specimen designated as S3 in Fig. 2a, can be observed for each C-CNP specimen prior to the rapid load drop indicative of unstable crack growth. For F-CNP specimens, on the other hand, the load–deflection plots are noticeably nonlinear (circled in blue) as the crack initiation load is approached and

Table 1 Average tension characteristics of C-CNP and F-CNP

	E (GPa)	υ	Strength (Mpa)	Failure strain (%)
C-CNP	10.9 $\pm$ 0.4	0.28 $\pm$ 0.01	79 $\pm$ 8	3.0 $\pm$ 0.9
F-CNP	10.8 $\pm$ 0.3	0.23 $\pm$ 0.04	90 $\pm$ 8	4.0 $\pm$ 0.4

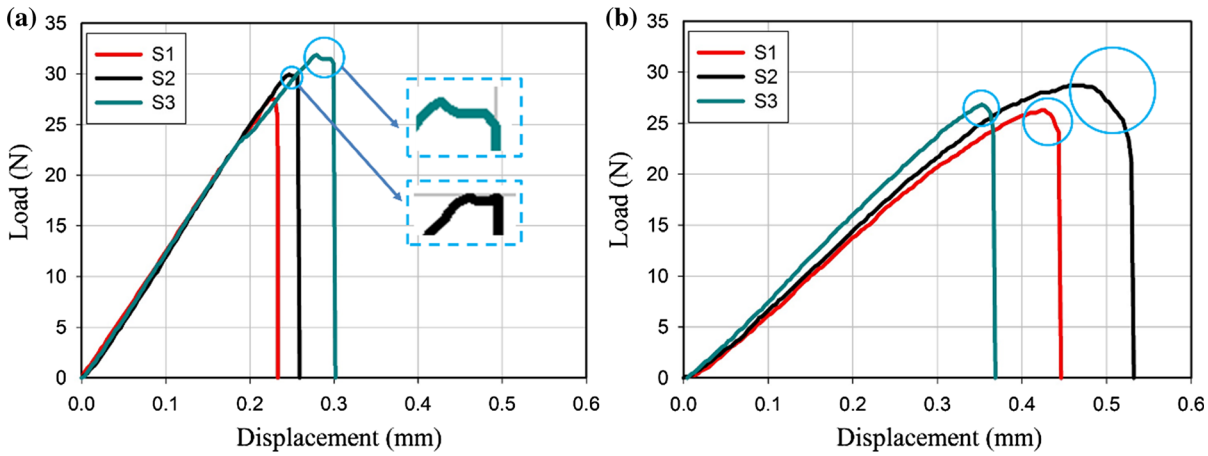

Fig. 2 Load-(load-point) deflection responses from three quasi-static fracture tests for **a** C-CNP, **b** F-CNP

Table 2 Fracture properties of C-CNP and F-CNP

	SIF at crack initiation, K_{Ic} (MPa $m^{1/2}$)	Far-field critical stress, σ_{cr} (MPa)	Critical G_c (kN/m)
C-CNP (B = 60 ± 3 μm)	4.6 ± 0.2	32.3 ± 1.8	1.9 ± 0.2
F-CNP (B = 40 ± 3 μm)	6.2 ± 0.3	44.0 ± 2.0	3.6 ± 0.3

subsequent drop is rather gradual after attaining critical/peak load. These qualitative observations suggest a failure process unique to material processing of these CNPs.

The mode-I stress intensity factors (SIF), K_I, were calculated under the assumption of small scale yielding from the measured load up to crack initiation using the equation (Tada et al. 2000):

$$K_I = \frac{P}{B \cdot w} \cdot \sqrt{\pi a} \cdot f\left(\frac{a}{w}\right) \quad (1)$$

where $f\left(\frac{a}{w}\right) = 1.122 - 0.231\left(\frac{a}{w}\right) + 10.55\left(\frac{a}{w}\right)^2 - 21.71\left(\frac{a}{w}\right)^3 + 30.38\left(\frac{a}{w}\right)^4$, P is the load, B is the nominal thickness of CNP, w is the width of the specimen and a is the initial crack length. The crack initiation toughness, also known as the critical SIF (K_{Ic}), was calculated using the measured load at crack initiation. The crack initiation toughness, critical stress (at crack initiation), strain energy release rate, G_{cr} $(= \frac{K_{Ic}^2}{E})$, obtained from the average values of multiple specimens for C-CNP and F-CNP are summarized in Table 2.[1] All the values for F-CNP are significantly larger than those for C-CNP suggesting an improvement of the fracture characteristics of CNP made from filtration technique.

The speckle images recorded during the experiment were analyzed using 2D-DIC to extract in-plane displacement components, u (x, y) and v (x, y) in the x- and y-directions, respectively, parallel and perpendicular to the initial crack. During quasi-static tests, the effects including rigid body motion and initial wrinkles on the specimen surface were considered. To minimize these effects, images with a small pre-load were selected as reference images, and the rest of the images were correlated with that reference using ARAMIS® image analysis software. Speckle images were segmented into sub-images or facets of size of 50 × 50 pixels (1 pixel corresponds to ∼ 12 μm on the specimen) with 40 pixels overlap (or 10 pixel steps) was used to extract the local displacement of speckles in approx. 30 × 20 mm^2 region-of-interest (ROI).

The specimen S3 for both C-CNP and F-CNP were selected to extract full-field displacements in the crack-tip vicinity. The speckle images along with the

[1] It is worth noting that values of SIF at crack initiation of C-CNP are comparable to conventional tough polymers such as bulk polycarbonate (K_{Ic} = 3–4 MPa$\sqrt{m}$) which offers lower elastic modulus (E = 2.5 GPa). The same for F-CNP are substantially higher, by 50%, suggesting a clear superiority in terms of crack initiation.

corresponding crack-opening displacement (displacement component along the *y*-axis) contours for C-CNP and F-CNP for a few select time instants are shown in Figs. 3 and 4, respectively. In these plots, t = 0 s corresponds to visually detectable crack initiation at the original notch-tip and the color-bars represent displacements in mm. It can be observed in Fig. 3 that, due to the symmetric nature of mode-I deformations, the crack is expected to propagate in a self-similar fashion or along the initial crack plane (from right to left in these images) and hence the *v*-displacement contours are generally symmetric in shape relative to the crack. When compared to isotropic elastic materials (Jajam et al. 2013), however, the displacement contours, particularly those behind the crack-tip, are somewhat asymmetric. That is, more contours on the upper half of the specimen (attached to the moving crosshead) when compared to the lower half (attached to the fixed crosshead). Tests on other specimens have produced similar results despite exercising sufficient care to avoid occurrence of twisting during tests. This suggests a deformation mechanism unique to CNP that produces such an out-of-plane deflection of crack flanks due to fiber entanglement observed in the micrographs and needs further investigation.

The *v*-displacement field contours for F-CNP in Fig. 4 also show a lack of symmetry in terms of number of contours relative to the initial crack plane, although dominant mode-I fracture occurred during tests. It can be observed from the right column in Fig. 4 that the contours below the initial crack are denser than those above the initial crack while upper and lower parts connected to the moving and fixed crossheads, respectively, as before. Again, the bottom right flank of F-CNP has undergone an out-of-plane deformation, noticeable from the speckle images in left column in Fig. 4. Again, this phenomenon was noticed for all the F-CNP specimens.

The back surface of each specimen S3 in the C-CNP and F-CNP categories was photographed using an optical microscope and are shown in Fig. 5. A narrow strip of whitened region, marked by yellow braces in the figure, was observed along the two crack flanks on both types of specimens. (It should be noted that this was observed in all specimens, although one example for each type is presented here; further, in each case the whitened region corresponding the nonlinear portion of the load–deflection plot (Fig. 2) was followed by a non-whitened region where unstable crack growth occurred). This inelastic, craze-like phenomenon in terms of appearance, similar to the one often seen in traditional engineering polymers, effectively increases the resistance of the material to crack growth. Furthermore, the length of the whitened zone of F-CNP is noticeably longer than that seen in C-CNP, which corresponds to the curves in Fig. 2 where the drop in load is more gradual/graceful for F-CNP than that for C-CNP. The fractured specimen edges of both C-CNP and F-CNP specimens were observed at higher magnifications using a high magnification digital microscope (KEYENCE VHX-6000 series microscope) and are shown in Fig. 6. (The heavy downward arrow indicates the global crack growth in the *x*-direction in the *x*–*y* plane, as shown in Fig. 5.) The micrographs in the top row correspond to the region where whitening was evident whereas the ones in the bottom row are for regions where whitening was not visible. In the latter images (bottom row) the crack edges are relatively smooth with no strong evidence of CNP fiber bridges across the crack faces. However, highly fibrous and more tortuous crack path in the whitened region of the two CNPs are readily evident in the former. When C-CNP images are compared to F-CNP, particularly in the whitened region, strong evidence of fiber bridging besides slightly broader craze-like strips all along and adjacent to the crack faces can be seen. As noted in Table S1, the F-CNP showed a slightly higher density (1225 kg/m^3) when compared to the C-CNP counterpart (1073 kg/m^3), potentially contributing to the above differences in crack growth morphology. This could also be observed from Fig. S9, the F-CNP displays a much more compact structure than C-CNP.

Since DIC captured the images during crack growth involving crack face fiber bridges in the whitened region, the fracture parameters—SIFs and energy release rates—in the post-crack initiation regime were also extracted under small scale yielding assumption. The crack-opening displacement fields (or the *v*-displacement field) were used to calculate the stress intensity factors (SIFs) using an over-deterministic least-squares analysis of measurements. The asymptotic expression for the *v*-field around the crack-tip can be expressed as (Kirugulige and Tippur 2009):

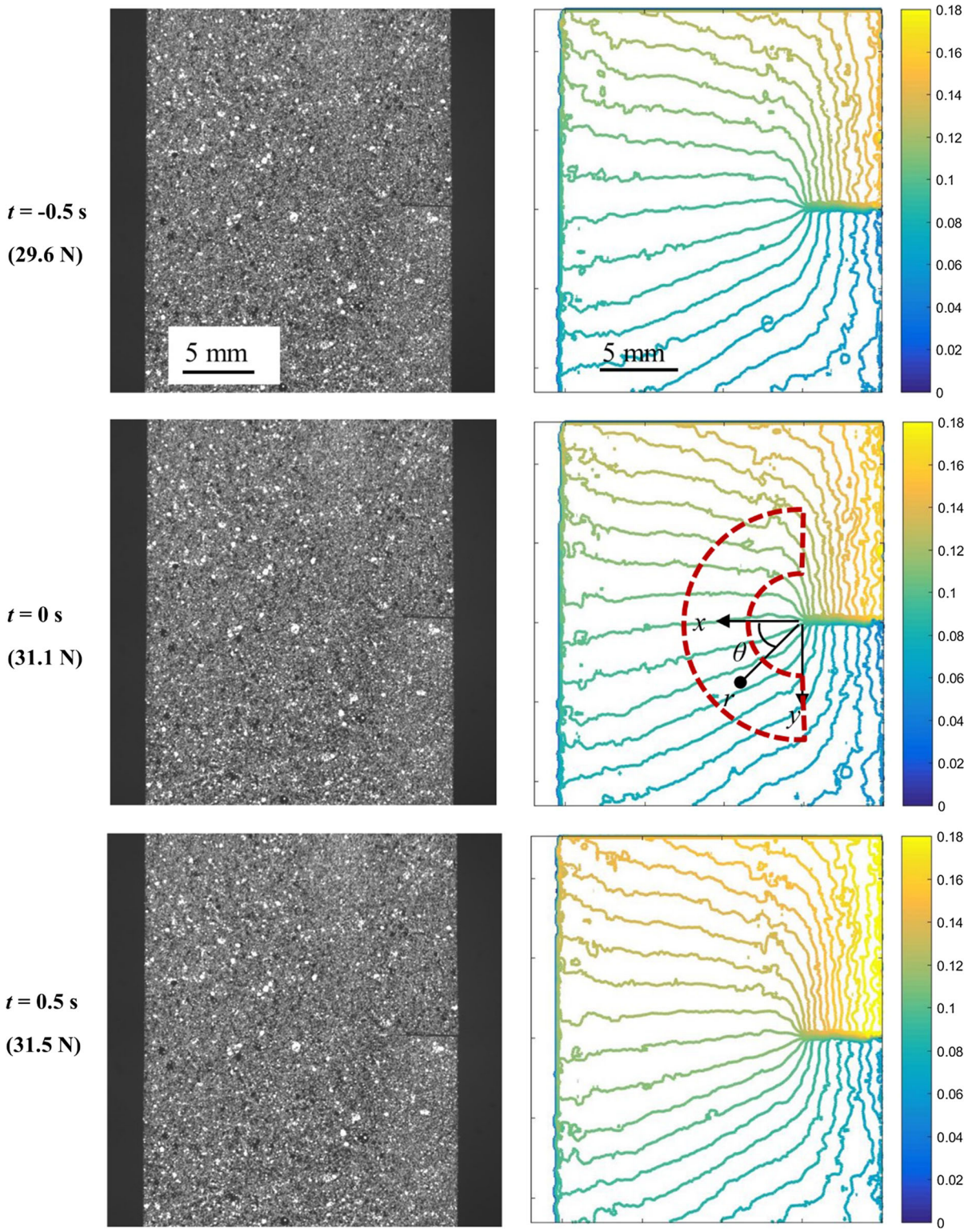

Fig. 3 Speckle images (left column) around crack initiation with corresponding measured crack-opening displacement contours (right column) for C-CNP. Contours are shown in 5 μm increments and the color bar scale is in mm

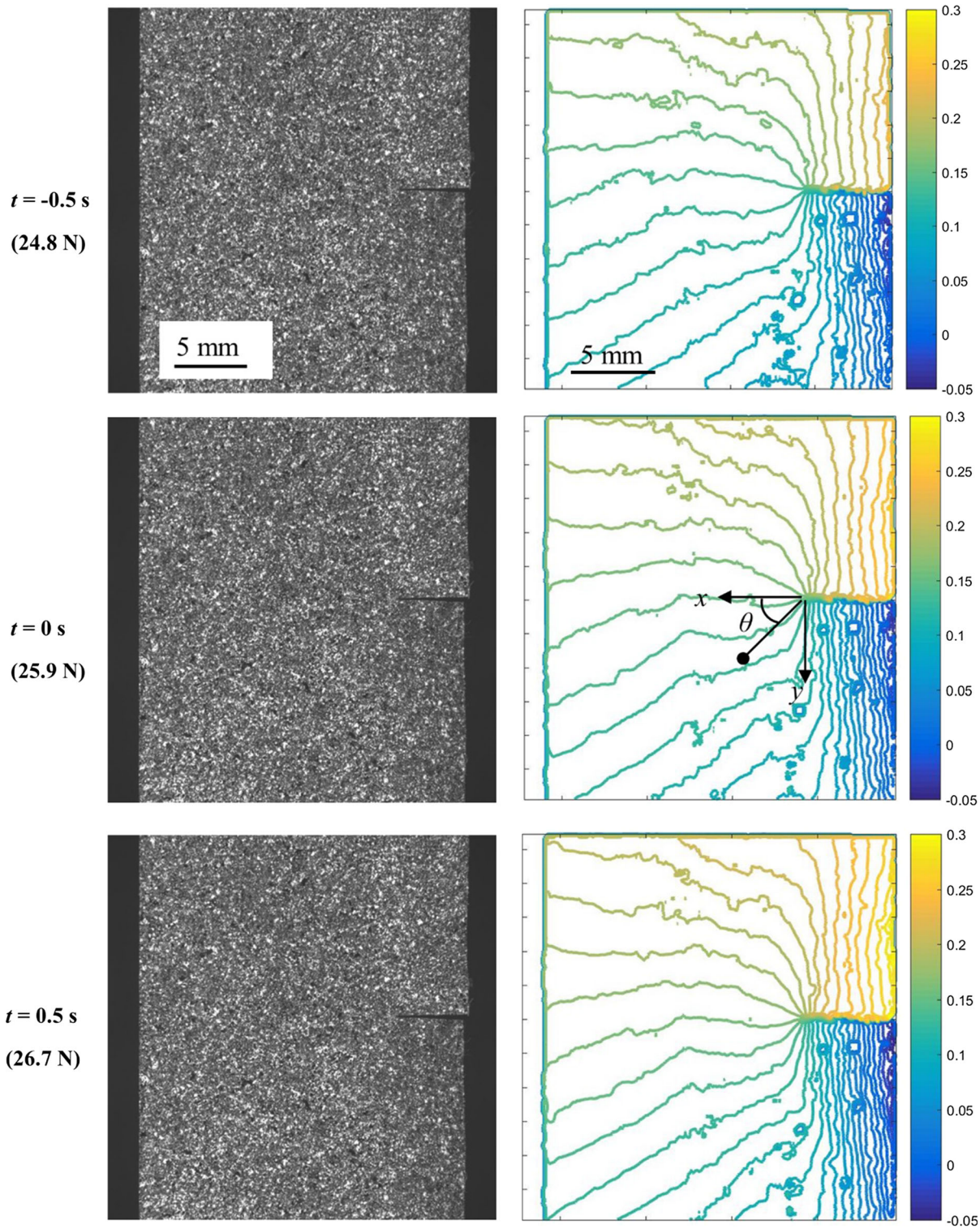

Fig. 4 Speckle images (left column) close to crack initiation load with corresponding measured crack-opening displacement contours (right column) for F-CNP. Contours are shown in 10 μm increments and the color bar scale is in mm

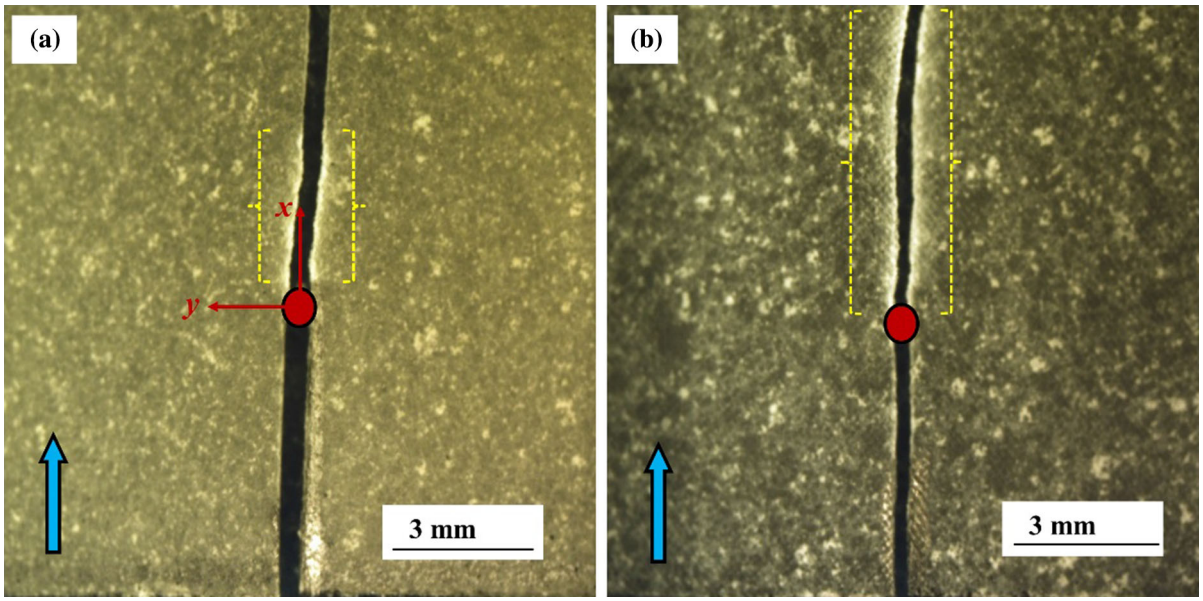

Fig. 5 Images of back surface of specimen S3 for C-CNP (**a**) and F-CNP (**b**). The blue arrow indicates crack growth direction, the yellow braces highlight the whitened/craze-like zone ahead of the initial crack tip, and the red dot indicates the initial crack tip. The whitened zone is noticeably short in **a** when compared to **b**

$$v(r,\theta) = \sum_{n=1}^{\infty} \frac{(K_I)_n}{2\mu}\frac{r^{n/2}}{\sqrt{2\pi}}\left\{\kappa \sin\frac{n}{2}\theta + \frac{n}{2}\sin\left(\frac{n}{2}-2\right)\theta - \left[\frac{n}{2}+(-1)^n\right]\sin\frac{n}{2}\theta\right\} + \sum_{n=1}^{\infty} \frac{(K_{II})_n}{2\mu}\frac{r^{n/2}}{\sqrt{2\pi}}\left\{-\kappa\cos\frac{n}{2}\theta - \frac{n}{2}\cos\left(\frac{n}{2}-2\right)\theta + \left[\frac{n}{2}-(-1)^n\right]\cos\frac{n}{2}\theta\right\} \quad (2)$$

where v is the crack-opening displacement, $(r,\ \theta)$ denotes the crack-tip polar coordinates as shown in Fig. 3, $\kappa(=\frac{3-\upsilon}{1+\upsilon})$ for plane stress, μ and υ are shear modulus and Poisson's ratio, respectively. In the above equation, K_I and K_{II} denote the mode-I and -II SIFs, respectively. Here, the analysis utilized discrete v-field data in the region around the crack-tip, 3 mm $\leq r \leq$ 6 mm, $-90° \leq \theta \leq 90°$ (in the sector shown by dotted lines in Fig. 3) in order to minimize the uncertainty associated with the precise crack-tip location yet sufficiently close to the crack-tip where Eq. (2) holds. The effect of non-singular far-field deformations if any on the measured K_I and K_{II} was offset by using four higher order terms (n = 4) in Eq. (2) during least-squares analysis. It should also be noted that the crack-tip displacements were forced to be zero during the analysis.

The DIC results (v-field) of each specimen for C-CNP and F-CNP were used to evaluate SIFs before and after crack initiation. The mode-I SIFs in the pre-crack initiation regime were comparatively examined relative to the theoretical counterparts calculated from Eq. (1). The mode-I SIFs are compared at load of every 3 N until fracture occurs in the specimen. The comparison is shown in Figs. 7a and b for both C-CNP and F-CNP specimens, respectively. The mode-I fracture toughness (or the crack initiation toughness) for C-CNP is $\sim$ 4.8 MPa $m^{1/2}$, which is lower than $\sim$ 5.9 MPa $m^{1/2}$ for F-CNP. It is evident in Fig. 7 that there is a good agreement between the experimental and theoretical values of mode-I SIF, indicating the measurements from DIC are satisfactory. The mode-II SIF values are also plotted in these figures for completeness even though the loading is nominally mode-I. These values are small and negligible relative to mode-I counterparts. The non-zero values of K_{II} in fact help provide an estimation of potential errors due to the least-squares analysis approach used.

Next, the SIFs in the post-crack initiation regime were evaluated for C-CNP and F-CNP specimens. The results were used to calculate strain energy release

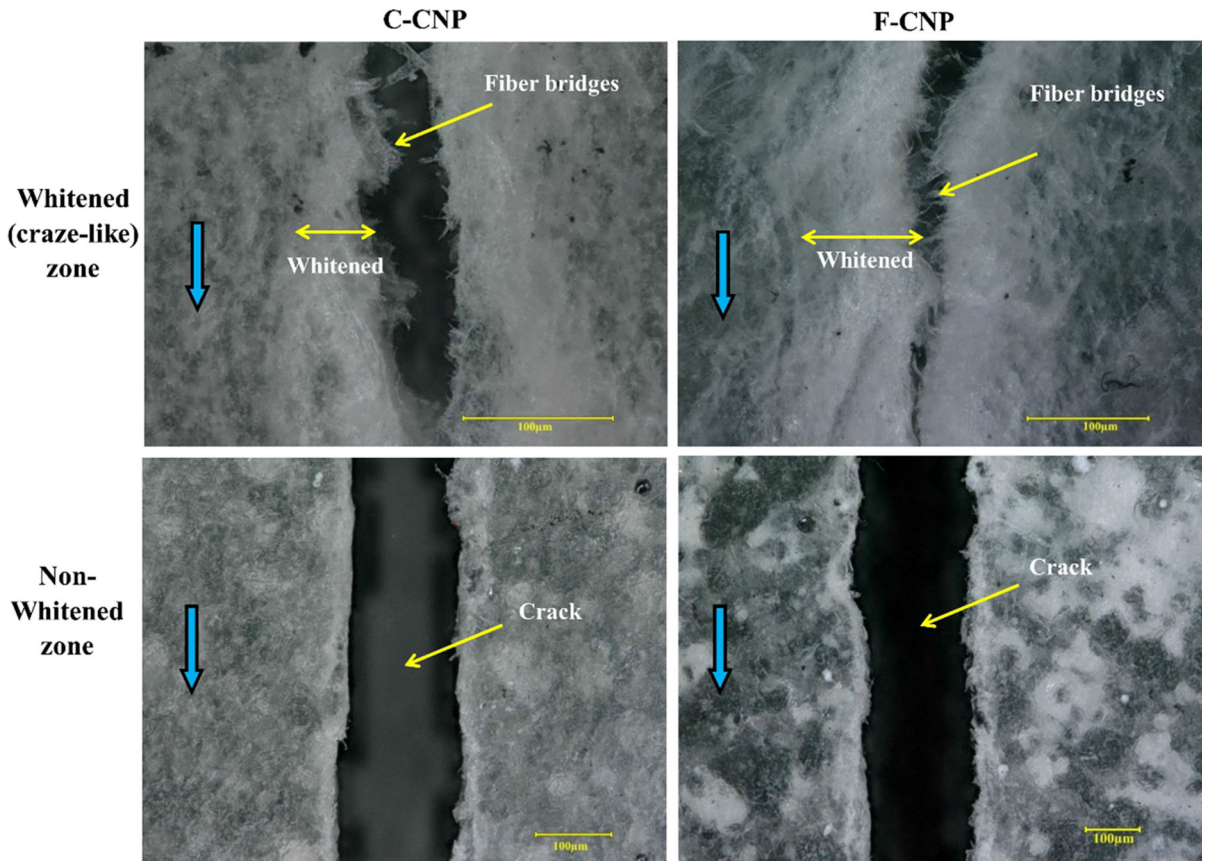

Fig. 6 Micrographs of fractured specimen edges of C-CNP and F-CNP. The blue arrow indicates the crack growth direction

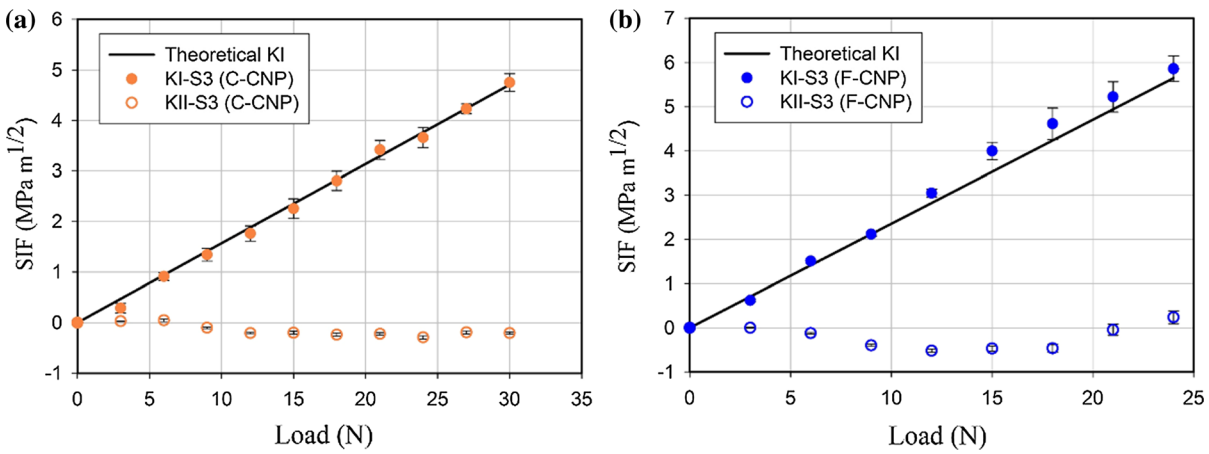

Fig. 7 Measured stress intensity factors (symbols) at different loads for C-CNP (**a**) and F-CNP (**b**). The solid line represents the corresponding theoretical values. Last data point in each set corresponds to values just prior to crack initiation, or K_{Ic}

rate, G ($=\frac{K_I^2+K_{II}^2}{E}$). Knowing the crack length at each load or displacement level during the experiments, plots of G versus a (crack length), or the so-called crack growth resistance curves, were obtained and are shown in Fig. 8. Specimens from both processing methods show increasing values of G during growth

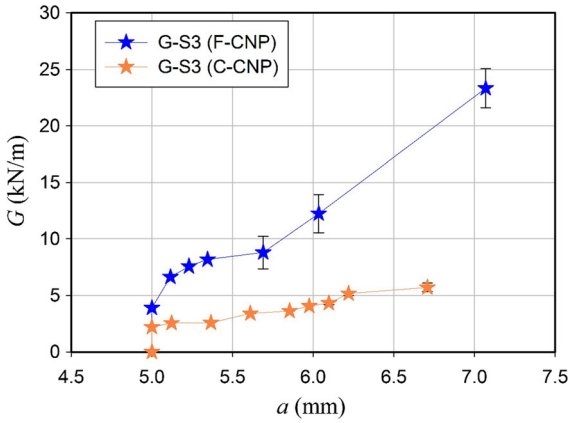

Fig. 8 Strain energy release rates for C-CNP and F-CNP in the post-crack initiation regime. Increasing trends imply resistance to crack growth

with the F-CNP displaying a desirable high resistance to growth relative to C-CNP. It can be observed that values of G for F-CNP increase from $\sim$ 3.9 to $\sim$ 23.3 kN/m within the observation window, they increase from $\sim$ 2.2 to $\sim$ 5.7 kN/m for C-CNP. Accordingly, from the crack growth resistance perspective the F-CNP are clearly superior to C-CNP counterparts, suggesting that the filtration method preferable to casting method.

Conclusions

A comparison of fracture properties of CNP made by casting and filtration methods is investigated in this work. The material properties of elastic modulus, strength and Poisson's ratio are obtained by performing tension tests on samples made of both types of CNP. The results show that both types of CNP have the similar elastic moduli, but F-CNP has higher strength. For quasi-static fracture tests, DIC was used to quantitatively visualize deformations in the crack vicinity by recording images before and after crack initiation in CNP. The crack opening displacements measured from DIC were used to calculate fracture parameters in the pre- and post-crack initiation regimes. The results show that crack growth resistance increases for both types of CNP in post-crack initiation regime. The F-CNP shows slightly higher ($\sim$ 20%) crack initiation toughness relative to C-CNP. Furthermore, both types of CNP show crack initiation toughness comparable to tough engineering polymers such as polycarbonate. A craze-like whitened zone ahead of the initial crack tip is observed along the crack flanks on both types of CNP during stable crack growth. The crack face fiber bridges and a relatively high crack path tortuosity are also evident in the whitened regions. This inelastic phenomenon effectively increases the resistance of CNP to crack growth. The craze-like zone in F-CNP is much longer than that in C-CNP, which is attributed to the cellulose nanofibers stacked tighter in F-CNP due to material processing. As a result, crack growth resistance increases much more significantly for F-CNP than for C-CNP, measured via crack growth resistance curves. The strain energy release rate increase is about sixfold in F-CNP whereas it is 2.5-fold in C-CNP during stable crack growth. Hence, filtration method is preferable to casting method to make CNP with better mechanical property, especially for the fracture property.

Acknowledgments Haishun Du acknowledges the financial support from the China Scholarship Council (No. 201708120052).

Compliance with ethical standards

Conflict of interest There is no conflict of interest.

References

Abdul Khalil HPS et al (2016) A review on nanocellulosic fibres as new material for sustainable packaging: process and applications. Renew Sustain Energy Rev 64:823–836. https://doi.org/10.1016/j.rser.2016.06.072

Abouzeid RE, Khiari R, El-Wakil N, Dufresne A (2018) Current state and new trends in the use of cellulose nanomaterials for wastewater treatment. Biomacromolecules 20:573–597. https://doi.org/10.1021/acs.biomac.8b00839

Aulin C, Gällstedt M, Lindström T (2010) Oxygen and oil barrier properties of microfibrillated cellulose films and coatings. Cellulose 17:559–574. https://doi.org/10.1007/s10570-009-9393-y

Benítez AJ, Walther A (2017) Cellulose nanofibril nanopapers and bioinspired nanocomposites: a review to understand the mechanical property space. J Mater Chem A 5:16003–16024. https://doi.org/10.1039/c7ta02006f

Bian H, Wei L, Lin C, Ma Q, Dai H, Zhu JY (2018a) Lignin-containing cellulose nanofibril-reinforced polyvinyl alcohol hydrogels. ACS Sustain Chem Eng 6:4821–4828. https://doi.org/10.1021/acssuschemeng.7b04172

Bian H, Gao Y, Wang R, Liu Z, Wu W, Dai H (2018b) Contribution of lignin to the surface structure and physical performance of cellulose nanofibrils film. Cellulose

25:1309–1318. https://doi.org/10.1007/s10570-018-1658-x

Bian H et al (2019) Recyclable and reusable maleic acid for efficient production of cellulose nanofibrils with stable performance. ACS Sustain Chem Eng 7:20022–20031. https://doi.org/10.1021/acssuschemeng.9b05766

Brhoum A, Dufresne A, Öhlund T, Samyn P (2017) Review of recent research on flexible multifunctional nanopapers: nanocellulose, electrospun nanofiber, and carbon-based nanopapers. Nanoscale 9:15181–15205. https://doi.org/10.1039/c7nr04656a

Chen W, Yu H, Lee SY, Wei T, Li J, Fan Z (2018) Nanocellulose: a promising nanomaterial for advanced electrochemical energy storage. Chem Soc Rev 47:2837–2872. https://doi.org/10.1039/C7CS00790F

Cheng Q, Ye D, Yang W, Zhang S, Chen H, Chang C, Zhang L (2018) Construction of transparent cellulose-based nanocomposite papers and potential application in flexible solar cells. ACS Sustain Chem Eng 6:8040–8047. https://doi.org/10.1021/acssuschemeng.8b01599

Chu TC, Ranson WF, Sutton MA (1985) Applications of digital-image-correlation techniques to experimental mechanics. Exp Mech 25:232–244. https://doi.org/10.1007/bf02325092

Diaz JA, Wu X, Martini A, Youngblood JP, Moon RJ (2013) Thermal expansion of self-organized and shear-oriented cellulose nanocrystal films. Biomacromolecules 14:2900–2908. https://doi.org/10.1021/bm400794e

Du H, Liu C, Zhang YD, Yu G, Si CL, Li B (2016) Preparation and characterization of functional cellulose nanofibrils via formic acid hydrolysis pretreatment and the followed high-pressure homogenization. Ind Crops Prod 94:736–745. https://doi.org/10.1016/j.indcrop.2016.09.059

Du H, Liu C, Zhang MM, Kong QS, Li B, Xian M (2018) Preparation and industrialization status of nanocellulose. Progr Chem 30:448–462. https://doi.org/10.7536/pc170830

Du H, Liu W, Zhang M, Si C, Zhang X, Li B (2019) Cellulose nanocrystals and cellulose nanofibrils based hydrogels for biomedical applications. Carbohydr Polym 209:130–144. https://doi.org/10.1016/j.carbpol.2019.01.020

Hu L et al (2018) Comparative evaluation of the efficient conversion of corn husk filament and corn husk powder to valuable materials via a sustainable and clean biorefinery process. ACS Sustain Chem Eng 7:1327–1336. https://doi.org/10.1021/acssuschemeng.8b05017

Jajam K, Bird S, Auad M, Tippur H (2013) Tensile, fracture and impact behavior of transparent Interpenetrating polymer networks with polyurethane-poly (methyl methacrylate). Polym Test 32:889–900. https://doi.org/10.1016/j.polymertesting.2013.04.010

Jiang F et al (2018) Wood-based nanotechnologies toward sustainability. Adv Mater 30:1703453. https://doi.org/10.1002/adma.201703453

Jung YH et al (2015) High-performance green flexible electronics based on biodegradable cellulose nanofibril paper. Nat Commun 6:7170. https://doi.org/10.1038/ncomms8170

Kargarzadeh H et al (2018) Recent developments in nanocellulose-based biodegradable polymers, thermoplastic polymers, and porous nanocomposites. Prog Polym Sci 87:197–227. https://doi.org/10.1016/j.progpolymsci.2018.07.008

Kirugulige MS, Tippur HV (2009) Measurement of fracture parameters for a mixed-mode crack driven by stress waves using image correlation technique and high-speed digital photography. Strain 45:108–122. https://doi.org/10.1111/j.1475-1305.2008.00449.x

Liu C et al (2017) Properties of nanocelluloses and their application as rheology modifier in paper coating. Ind Eng Chem Res 56:8264–8273. https://doi.org/10.1021/acs.iecr.7b01804

Luo H, Cha R, Li J, Hao W, Zhang Y, Zhou F (2019) Advances in tissue engineering of nanocellulose-based scaffolds: a review. Carbohydr Polym 224:115144. https://doi.org/10.1016/j.carbpol.2019.115144

Mao R, Goutianos S, Tu W, Meng N, Yang G, Berglund LA, Peijs T (2017) Comparison of fracture properties of cellulose nanopaper, printing paper and buckypaper. J Mater Sci 52:9508–9519. https://doi.org/10.1007/s10853-017-1108-4

Mautner A, Lee K-Y, Tammelin T, Mathew AP, Nedoma AJ, Li K, Bismarck A (2015) Cellulose nanopapers as tight aqueous ultra-filtration membranes. React Funct Polym 86:209–214. https://doi.org/10.1016/j.reactfunctpolym.2014.09.014

Meng Q, Li B, Li T, Feng X-Q (2017) A multiscale crack-bridging model of cellulose nanopaper. J Mech Phys Solids 103:22–39. https://doi.org/10.1016/j.jmps.2017.03.004

Meng Q, Li B, Li T, Feng X-Q (2018) Effects of nanofiber orientations on the fracture toughness of cellulose nanopaper. Eng Fract Mech 194:350–361. https://doi.org/10.1016/j.engfracmech.2018.03.034

Miao C, Tippur HV (2019) Fracture behavior of carbon fiber reinforced polymer composites: an optical study of loading rate effects. Eng Fract Mech 207:203–221. https://doi.org/10.1016/j.engfracmech.2018.12.035

Mohammed N, Grishkewich N, Tam KC (2018) Cellulose nanomaterials: promising sustainable nanomaterials for application in water/wastewater treatment processes. Enviro Sci Nano 5:623–658. https://doi.org/10.1039/c7en01029j

Nogi M, Karakawa M, Komoda N, Yagyu H, Nge TT (2015) Transparent conductive nanofiber paper for foldable solar cells. Sci Rep 5:17254. https://doi.org/10.1038/srep17254

Operamolla A, Casalini S, Console D, Capodieci L, Di Benedetto F, Bianco GV, Babudri F (2018) Tailoring water stability of cellulose nanopaper by surface functionalization. Soft Matter 14:7390–7400. https://doi.org/10.1039/c8sm00433a

Parit M, Aksoy B, Jiang Z (2018) Towards standardization of laboratory preparation procedure for uniform cellulose nanopapers. Cellulose 25:2915–2924. https://doi.org/10.1007/s10570-018-1759-6

Qing Y, Sabo R, Wu Y, Zhu JY, Cai Z (2015) Self-assembled optically transparent cellulose nanofibril films: effect of nanofibril morphology and drying procedure. Cellulose 22:1091–1102. https://doi.org/10.1007/s10570-015-0563-9

Rol F, Belgacem MN, Gandini A, Bras J (2019) Recent advances in surface-modified cellulose nanofibrils. Prog

Polym Sci 88:241–264. https://doi.org/10.1016/j.progpolymsci.2018.09.002

Sehaqui H, Liu A, Zhou Q, Berglund LA (2010) Fast preparation procedure for large, flat cellulose and cellulose/inorganic nanopaper structures. Biomacromolecules 11:2195–2198. https://doi.org/10.1021/bm100490s

Shrestha S, Diaz JA, Ghanbari S, Youngblood JP (2017) Hygroscopic swelling determination of cellulose nanocrystal (CNC) films by polarized light microscopy digital image correlation. Biomacromolecules 18:1482–1490. https://doi.org/10.1021/acs.biomac.7b00026

Sun X, Wu Q, Ren S, Lei T (2015) Comparison of highly transparent all-cellulose nanopaper prepared using sulfuric acid and TEMPO-mediated oxidation methods. Cellulose 22:1123–1133. https://doi.org/10.1007/s10570-015-0574-6

Sun W, Tajvidi M, Hunt CG, McIntyre G, Gardner DJ (2019) Fully bio-based hybrid composites made of wood, fungal mycelium and cellulose nanofibrils. Sci Rep 9:3766. https://doi.org/10.1038/s41598-019-40442-8

Tada H, Paris P, Irwin G (2000) The analysis of cracks handbook, vol 2. ASME Press, New York, p 1

Thomas B et al (2018) Nanocellulose, a versatile green platform: from biosources to materials and their applications. Chem Rev 118:11575–11625. https://doi.org/10.1021/acs.chemrev.7b00627

Wang Q et al (2018) Flexible cellulose nanopaper with high wet tensile strength, high toughness and tunable ultraviolet blocking ability fabricated from tobacco stalk via a sustainable method. J Mater Chem A 6:13021–13030. https://doi.org/10.1039/c8ta01986j

Wang L, Palmer J, Tajvidi M, Gardner DJ, Han Y (2019) Thermal properties of spray-dried cellulose nanofibril-reinforced polypropylene composites from extrusion-based additive manufacturing. J Therm Anal Calorim 136:1069–1077. https://doi.org/10.1007/s10973-018-7759-9

Xie H, Du H, Yang X, Si C (2018) Recent strategies in preparation of cellulose nanocrystals and cellulose nanofibrils derived from raw cellulose materials. Int J Polym Sci 2018:1–25. https://doi.org/10.1155/2018/7923068

Xing J, Tao P, Wu Z, Xing C, Liao X, Nie S (2019) Nanocellulose-graphene composites: a promising nanomaterial for flexible supercapacitors. Carbohydr Polym 207:447–459. https://doi.org/10.1016/j.carbpol.2018.12.010

Yang W, Jiao L, Min D, Liu Z, Dai H (2017) Effects of preparation approaches on optical properties of self-assembled cellulose nanopapers. RSC Adv 7:10463–10468. https://doi.org/10.1039/C6RA27529J

Zhao M, Ansari F, Takeuchi M, Shimizu M, Saito T, Berglund LA, Isogai A (2017) Nematic structuring of transparent and multifunctional nanocellulose papers. Nanoscale Horiz. https://doi.org/10.1039/c7nh00104e

Zheng T, Zhang Z, Shukla S, Agnihotri S, Clemons CM, Pilla S (2019) PHBV-graft-GMA via reactive extrusion and its use in PHBV/nanocellulose crystal composites. Carbohydr Polym 205:27–34. https://doi.org/10.1016/j.carbpol.2018.10.014

Zhu H et al (2013) Biodegradable transparent substrates for flexible organic-light-emitting diodes. Energy Environ Sci 6:2105. https://doi.org/10.1039/c3ee40492g

Zhu H et al (2015) Anomalous scaling law of strength and toughness of cellulose nanopaper. Proc Natl Acad Sci U S A 112:8971–8976. https://doi.org/10.1073/pnas.1502870112

Zhu H et al (2016) Wood-derived materials for green electronics, biological devices, and energy applications. Chem Rev 116:9305–9374. https://doi.org/10.1021/acs.chemrev.6b00225

Publisher's Note Springer Nature remains neutral with regard to jurisdictional claims in published maps and institutional affiliations.